

CFD Computation of Flow Fractional Reserve (FFR) in Coronary Artery Trees Using a Novel Physiologically Based Algorithm (PBA) Under 3D Steady and Pulsatile Flow Conditions

Nursultan Alzhanov¹, Eddie Y. K. Ng², Xiaohui Su³, Yong Zhao^{1*}

¹ Mechanical and Aerospace Engineering Department, School of Engineering, Nazarbayev University, Asana 010000, Kazakhstan; nursultan.alzhanov@nu.edu.kz

² School of Mechanical and Aerospace Engineering, Nanyang Technological University: Singapore 639798, Singapore; mykng@ntu.edu.sg

³ School of Mechanical Engineering, Dalian University of Technology, China; sxh@dlut.edu.cn

* Correspondence: yong.zhao@nu.edu.kz

Abstract: A novel physiologically based algorithm (PBA) for the computation of fractional flow reserve (FFR) in coronary artery trees (CATs) using computational fluid dynamics (CFD) is proposed and developed. The PBA is based on the extension of Murray's law and additional inlet conditions prescribed iteratively, and is implemented in OpenFOAM for testing and validation. 3D models of CATs are created using CT scans and computational meshes, and the results are compared to invasive coronary angiographic (ICA) data to validate the accuracy and effectiveness of the PBA. The discrepancy between calculated and experimental FFR is within 2.33–5.26% in steady-state and transient simulations, respectively, when convergence is reached. The PBA is a reliable and physiologically sound technique compared to the current lumped parameter model (LPM), which is based on empirical scaling correlations and requires nonlinear iterative computing for convergence. The accuracy of the PBA method is further confirmed using the FDA nozzle, which demonstrates good alignment with CFD-validated values.

Keywords: FFR, Blood Flow Simulation, coronal stenosis, Coronary Computed Tomography Angiography (CCTA), OpenFOAM.

1. Introduction

The coronary artery is one of the essential blood arteries that ensure the heart receives a steady blood flow. The heart muscle (myocardium) receives oxygenated blood via the coronary arteries; when these are clogged or obstructed, the myocardium starts to deteriorate, a condition known as ischemia. The most significant cause of death worldwide is coronary artery disease (CAD), also known as ischemic heart disease. According to a report by the World Health Organization, CAD causes nearly 50% of disease-related death in Kazakhstan [1]. An American will experience a coronary episode roughly every 25 seconds; statistically, the pass-away rate is approximately every minute [2].

Coronary angiography may offer information on anatomical stenosis, the gold standard for diagnosing coronary heart disease. Evaluations of fractional flow reserve (FFR) from CT in Europe and the United States suggest that it has the potential to decrease false diagnoses before patients are referred for invasive testing [3].

Coronary artery computerized tomography (CT) imaging is preferred over coronary angiography for pre-screening asymptomatic individuals. Due to its noninvasive nature, ease of use, cheap cost, and excellent repeatability. Since FFR from CT is based on high-quality coronary artery CT angiography (CTA) image data, it doesn't need extra load, scanning, or dosage. Although there is a grey area that necessitates additional functional measures for diagnosis, the diagnostic accuracy and specificity are greater than those of coronary artery CT imaging. The quantitative coronary artery CT imaging index may objectively identify functional coronary stenosis [4].

Compared to angiography alone, FFR is one of the few diagnostic tools that can effectively lead therapeutic approaches, improve safety and efficacy, and reduce costs. The angio-FFR, a noninvasive estimate of FFR generated from computed tomography coronary angiography, employs specialized software to model the 3-dimensional coronary blood flow. The DISCOVER-FLOW research revealed an 84.3 percent diagnosis accuracy for lesions contextually assessed using FFR. Similarly, the HEARTFLOW-NXT research found an 86 percent per-vessel diagnosis accuracy [5].

As an optional tool for hemodynamic evaluation in patients with single-vessel CAD, the excellent diagnostic accuracy of SPECT CFR for diagnosing functionally significant stenosis justifies its usage. SPECT CFR was supported by superior diagnostic accuracy for identifying functionally significant stenosis. An aberrant CFR may suggest microvascular dysfunction in individuals whose FFR and CFR differ, which needs more research [6].

The CT scans may be used to construct three-dimensional (3D) solid models that can be seen on display, printed on film or by a 3D printer, or used by a Computational Fluid Dynamics (CFD) approach that enables doctors to quantify the coronary physiology inside the artery. Current CFD programs that have undergone clinical examination in significant clinical investigations include Discover Flow, HeartFlow - NXT, and other Platforms for the physiologic study of coronary artery function [7]. Additionally, using CFD to estimate FFR has been offered as a potential noninvasive alternative to Fractional Flow Reserve Invasive Coronary Angiography measurement [8].

Consequently, computational analysis of FFR utilizing CCTA imaging data enables noninvasive lesion-specific decline assessment. This anatomical and functional assessment may identify people with lesion-causing coronary pressure decreases. This noninvasive approach may be superior to invasive ICA with FFR for patient treatment. We need more information on incorporating the new strategy into "real-world" clinical practice to influence future patient care decisions [9].

Instead of simulating maximum hyperemia, boundary conditions are specified to create a pressure-flow curve for stenosis. Then, stenosis is functionally diagnosed using pressure-flow curve characteristics. The suggested strategy is verified with invasive FFR in six individuals using idealized and patient-specific models. According to the results, stenosis flow resistances cannot be directly acquired from anatomy. Simulated pressure-flow parameters correlate linearly and significantly with invasive FFR. The suggested technique may estimate flow resistances using pressure flow from curve-derived parameters. Furthermore, flow resistances can be assessed without modeling maximum hyperemia [10].

However, since a cardiac tree often includes multiple capillary branches connecting with downstream microcirculation, it is almost impossible to measure the outflow border conditions experimentally owing to their tiny branch diameters. Consequently, the Windkessel-type boundary conditions are based on the so-called Lumped Parameter Model (LPM) and the more complex Lumped Parameter Network Model (LPNM). Both methods are typically adopted in approximating the outflow boundary conditions that represent the highly complex dynamic interactions between the tree and its downstream microvasculature. These approaches are based on the circuit analogy theory, which necessitates the measurement of resistances, capacitances, and empirical correlations, which are sometimes challenging to compute without patient-specific data and are not physiologically grounded. The connection of the generated Ordinary Differential Equations (ODEs) from these approaches with the CFD solver also creates unclear boundary conditions, which may often result in slow convergence or even divergence of numerical solutions [11,12].

The problem addressed in this work is the diagnosis of stenosis (obstruction or narrowing) in the coronary arteries of individual patients. Traditional methods for diagnosing stenosis, such as coronary angiography, have limitations and can be invasive, costly, and carry risks for the patient. There is a need for more effective and noninvasive diagnostic methods for stenosis.

The PBA method proposed in this work is based on an extension of Murray's law and different inlet criteria [13], and is designed to be used alternately and iteratively to compute the outflow boundary conditions of the coronary tree for individual patients. The PBA method has been validated using FFR measurements in actual patient arteries and benchmarking with the FDA's nozzle. It is intended to provide realistic and tailored outflow boundary conditions for the diagnosis of stenosis without requiring measurable data. The unique contribution of the PBA method to the field is its use of Murray's law to establish initial boundary conditions that are then modified through the addition of new inlet boundary conditions and iterations, resulting in numerical convergence. This approach may provide a more effective and noninvasive method for diagnosing stenosis in the coronary arteries of individual patients.

In the cardiovascular system, an agreement between experiments and the Murray diameter model has been found only in small arteries [14] and arterioles [15,16], which is our CAD case. The final conditions at the outlets are ultimately decided by the tree's geometry, the conservation laws built into CFD, the numerical iterations, and the additional inlet patient-specific parameters; we only utilize Murray's formula to estimate their initial conditions. The third law may not accurately predict the outcome since we use it as a preliminary approximation.

Unlike machine learning-based data-driven simulation models, which depend on a significant quantity of data to verify, this PBA model is entirely based on physiology and physics. We are currently in the conceptual model-proof stage. It is undoubtedly desirable to undertake large-scale clinical testing, which we hope to accomplish in the next step for possible commercialization and future clinical uses. Because of this, we are doing model validation using experimental benchmark data and output from other simulations.

IREC did the study related to the patient's data collection and ethical approval.

2. Mathematical Formulations and Numerical Methods

2.1. Governing equations for hemodynamic flow

OpenFOAM is a software used to solve fluid flow problems by numerically solving the governing equations for blood flow using the SIMPLE and PIMPLE algorithms. These algorithms can be used to perform steady-state and transient simulations, respectively, and are capable of handling 3D laminar, turbulent, steady, and unsteady flows and compressible and incompressible flows. When calculating blood flow in OpenFOAM, the software uses the incompressible 3D Navier-Stokes (NS) equation to model the flow of the fluid.

$$\begin{aligned} \frac{\partial u}{\partial x} + \frac{\partial v}{\partial x} + \frac{\partial w}{\partial x} &= 0 \\ \rho \left(\frac{\partial u}{\partial t} + u \frac{\partial u}{\partial x} + v \frac{\partial u}{\partial y} + w \frac{\partial u}{\partial z} \right) &= -\frac{\partial P}{\partial x} + \rho g_x + \mu \left(\frac{\partial^2 u}{\partial x^2} + \frac{\partial^2 u}{\partial y^2} + \frac{\partial^2 u}{\partial z^2} \right) \\ \rho \left(\frac{\partial v}{\partial t} + u \frac{\partial v}{\partial x} + v \frac{\partial v}{\partial y} + w \frac{\partial v}{\partial z} \right) &= -\frac{\partial P}{\partial y} + \rho g_y + \mu \left(\frac{\partial^2 v}{\partial x^2} + \frac{\partial^2 v}{\partial y^2} + \frac{\partial^2 v}{\partial z^2} \right) \\ \rho \left(\frac{\partial w}{\partial t} + u \frac{\partial w}{\partial x} + v \frac{\partial w}{\partial y} + w \frac{\partial w}{\partial z} \right) &= -\frac{\partial P}{\partial z} + \rho g_z + \mu \left(\frac{\partial^2 w}{\partial x^2} + \frac{\partial^2 w}{\partial y^2} + \frac{\partial^2 w}{\partial z^2} \right) \end{aligned}$$

The above NS equations in Cartesian form are normally cast in tensor form for convenience:

$$\rho V_{i,t} + \rho v_j v_{i,j} - p_{,i} - \tau_{ij,j} = 0,$$

$$v_{i,i} = 0$$

(1)

ρ – density of blood, kg/m³

v_i – i component of velocity, m³/s
 $V_{i,t}$ – velocity derivative with respect to time
 p – pressure, Pa
 τ_{ij} – stress tensor (viscous portion)

OpenFOAM uses the Finite Volume Method (FVM) and SIMPLE/SIMPLEC/PISO pressure correction schemes to solve the Navier-Stokes equations for incompressible fluid flow. The domain of the equation is defined as Ω in three dimensions, and the boundary conditions are specified as $\Gamma = \Gamma_D \cup \Gamma_N$, where Γ_D represents Dirichlet boundary conditions and Γ_N represents Neumann boundary conditions. The domain is discretized using n_{el} linear unstructured tetrahedral elements, $\bar{\Omega}_e$. The final form of the equation is given by eq (2).

$$\begin{aligned}
 B_G(w_i, q; v_i, p) = & \int_{\Omega} \{w_i(\rho \dot{v}_i + \rho v_j v_{i,j}) + w_{i,j}(-\rho \sigma_{ij} + \tau_{ij}) - q_{,i} v_i\} d\Omega + \\
 & \int_{\Gamma_N} \{w_i(\rho \delta_{in} + \tau_{in}) + q v_{in}\} d\Gamma
 \end{aligned} \quad (2)$$

where $w \in W_n^k$ and $q \in P_h^k$

2.2 The Murray's law and PBA for rapid iterative computation of outlet conditions

The present work proposes a method that aims to address the problems related to the boundary conditions of the Windkessel type and provide patient-specific and realistic outflow boundary conditions in the absence of observed data. This method is based on an extension of Murray's law and the use of different inlet conditions that are alternately and iteratively applied. Sumbekova et al. previously carried out using commercial software [21]. It has been shown that vascular systems follow Murray's law, which states that mammalian vascular transport systems use minimum energy for blood maintenance and transport.

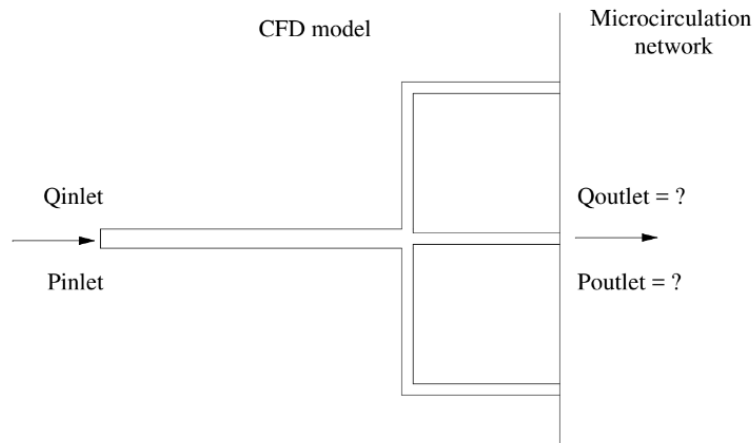


Figure 1. Schematic of the new boundary model.

According to the Hagen-Poiseuille Law for laminar flow in a vessel, the power required to drive a blood flow through it, is

$$P_t = \frac{8\mu l}{\pi r^4} \dot{Q}^2 \quad (3)$$

where \dot{Q} is the volumetric flow rate, l the length of the vessel, r its radius and μ the blood viscosity.

Furthermore, the power necessary for the maintenance of the blood in the vessel is proportional to the blood volume in the vessel:

$$V = \pi l r^2$$

The power required to maintain the metabolism in the blood is thus (4)

$$P_m = \lambda V = \lambda \pi l r^2 \quad (5)$$

where λ is the metabolic rate of the blood.

The total power required to drive the blood and maintain it, is

$$P = P_t + P_m = \frac{8\mu l}{\pi r^4} \dot{Q}^2 + \lambda \pi l r^2 \quad (6)$$

The radius that meets the minimum power requirement is obtained through the differentiation of P with respect to r and setting it to zero:

$$\frac{dP}{dr} = -\frac{32\mu l}{\pi r^5} \dot{Q}^2 + 2\lambda \pi l r = 0 \quad (7)$$

Thus

$$\dot{Q} = \frac{\pi}{4} r^3 \sqrt{\frac{\lambda}{\mu}} \quad (8)$$

Vessel radius and volumetric flow rate in individual vessels have this functional connection. In order to find the converged patient-specific flow outlet conditions in all of the outlets of a coronary tree for a given inlet pressure and volumetric flow rate that are prescribed alternatively through iterative computation, a novel iterative scheme is thus proposed to couple Murray's law with CFD simulation. For a particular branch i of a coronary tree with N branches as shown in Figure 1, its outflow is

$$\dot{Q}_i = \frac{\pi}{4} r_i^3 \sqrt{\frac{\lambda}{\mu}} \quad (9)$$

And according to the conservation law, we have

$$\dot{Q}_{in} = \sum_{i=1}^N \dot{Q}_i = \frac{\pi}{4} \sqrt{\frac{\lambda}{\mu}} \sum_{i=1}^N r_i^3 \quad (10)$$

Eq. (11) below can then be obtained by dividing Eq. (9) by Eq. (10) and rearranging it:

$$\dot{Q}_i = \frac{r_i^3}{\sum_{i=1}^N r_i^3} \dot{Q}_{in} \quad (11)$$

Our new physiologically based algorithm (PBA) aimed to extract personalized/patient-specific outflow boundary conditions. It represents the interactions between the coronary tree and its microcirculation network downstream under both steady and unsteady conditions are shown in a flowchart, as illustrated in Figure 2.

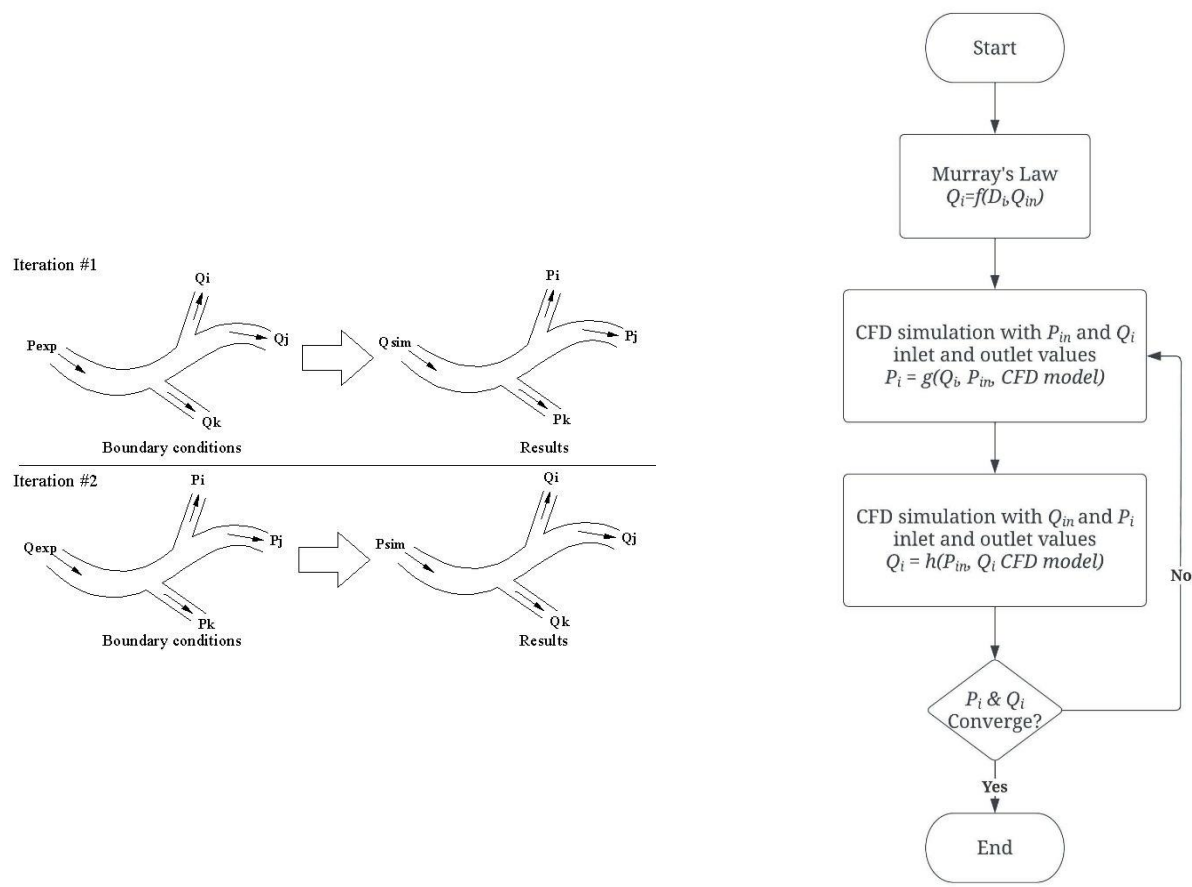


Figure 2. Algorithm for the outflow boundary conditions.

In this work, the above-mentioned methods are implemented in OpenFOAM to perform computational study of the hemodynamics in several patient specific geometries with the aim of validating the methods using related ICA measurements, such as inlet flow rate and pressure and FFR_{ICA} . There are four vascular cases, named as CT209, CHN13, CHN03 and FDA nozzle implemented by using the proposed PBA technique. Table 1 lists the workflow procedure for the PBA.

Table 1. Workflow procedure of Rapid Iterative algorithm.

Timestep	Initial conditions		Recorded	
	Inlet	Outlet	Inlet	Outlet
1 st round of iteration	p_{in} (table value) ^a	Q_i^*	Q_{2i}	p_{2i}
2 nd round of iteration	Q_{in} (table value) ^b	p_{2i}	p_{3i}	Q_{3i}
3 rd round of iteration	p_{in} (table value)	Q_{3i}	Q_{4i}	P_{4i}
...

i – is the number of coronary branches

^acalculated by Murray's law at beginning

^a Experimentally measured distal pressure at the inlet of blood vessel.

^b Experimentally measured flow rate at the inlet of blood vessel.

Q_{in} ; P_{in} ; Q_i ; P_i – CFD solver calculated values of pressure and flow rate at the inlet and outlets at different stages.

The geometries and their outlets of CT209, CHN13 and CHN03 are presented in Figs. 3-5 respectively.

Tables 2 to 4 present the experimental results of pressure and flow rate at the inlet of a vessel (aorta) for steady-state simulations of three artery models: CT209, CHN13, and CHN03. Similarly, Tables 5 to 7 display the initial flow rates at the outlets of the three artery models, which are calculated using equation 11 based on Murray's law, with the inlet and outlet boundary conditions specified in Table 1. Figure 6 presents the inlet values for the transient case. The time-averaged value of the inlet waveform for the transient scenario was compared to the steady-state case to ensure the accuracy of the comparison.

In this study, the same set of fluid properties and blood model were used for both steady-state and transient simulations. The properties included a Newtonian dynamic viscosity of 0.0035 Ns/m² and a density of 1056 kg/m³ [18]. The boundary conditions for these simulations included velocity/pressure inlets and velocity/pressure outlets, which were iteratively switched as part of the PBA scheme. The blood flow was modeled as laminar fluid flow. To ensure convergence, the criteria for the transient simulations required that the residual reduction must be lower than five orders of magnitude, ranging from 1 down to 10⁻⁵, while the criteria for the steady-state simulations required that the residual reduction must be lower than 10⁻³. In addition, the inlet data provided for each artery indicated that two cycles were used in the transient case.

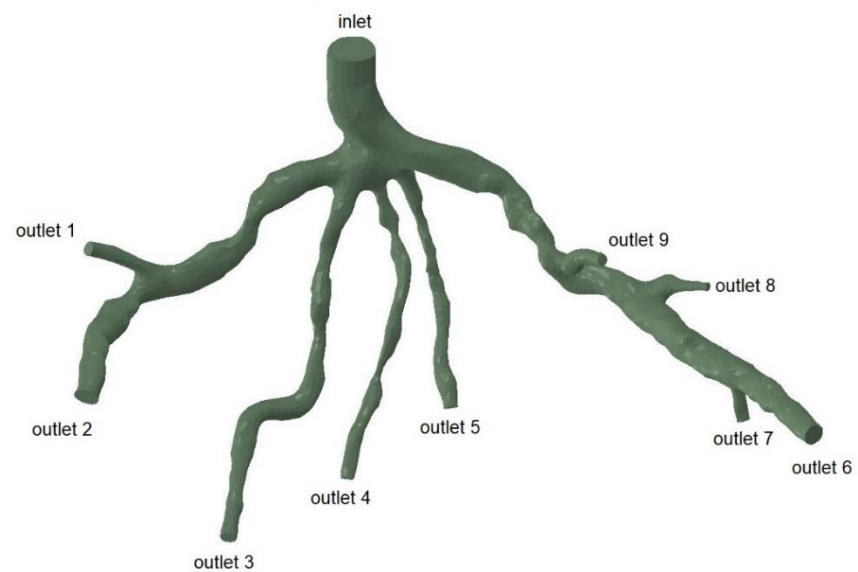


Figure 3. Geometry and Inlet/Outlets of the CT209 model

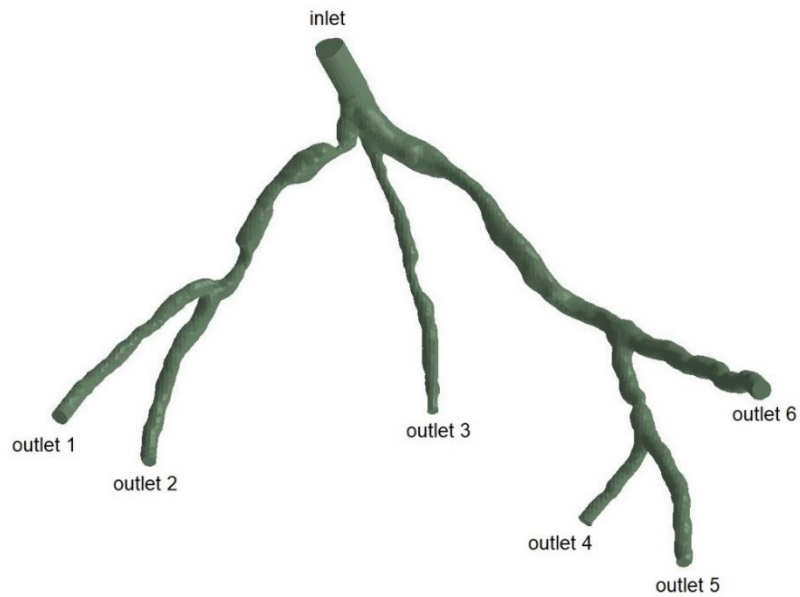


Figure 4. Geometry and Inlet/Outlets of the CHN13 model

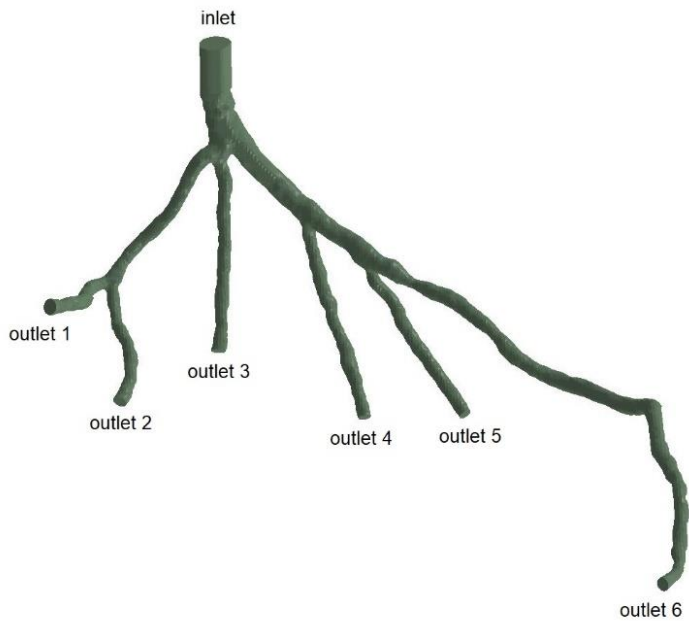


Figure 5. Geometry and Inlet/Outlets of the CHN03 model

Table 2. Experimentally obtained input parameters for simulation for CT209

Parameter	Value
Experimental inlet pressure P_{exp}	90.53 mm Hg (12070.12 Pa)
Experimental inlet flow rate Q_{exp}	9.39944 cm ³ /s

Table 3. Experimentally obtained input parameters for simulation for CHN13

Parameter	Value
Experimental inlet pressure P_{exp}	90.61 mm Hg (12870.12 Pa)
Experimental inlet flow rate Q_{exp}	7.17551 cm ³ /s

Table 4. Experimentally obtained input parameters for simulation for CHN03.

Parameter	Value
Experimental inlet pressure P_{exp}	76.5 mm Hg (10201.9 Pa)
Experimental inlet flow rate Q_{exp}	6.18 cm ³ /s

Table 5. Initial calculated flow rates at each outlet by Murray's law for CT209 [21]

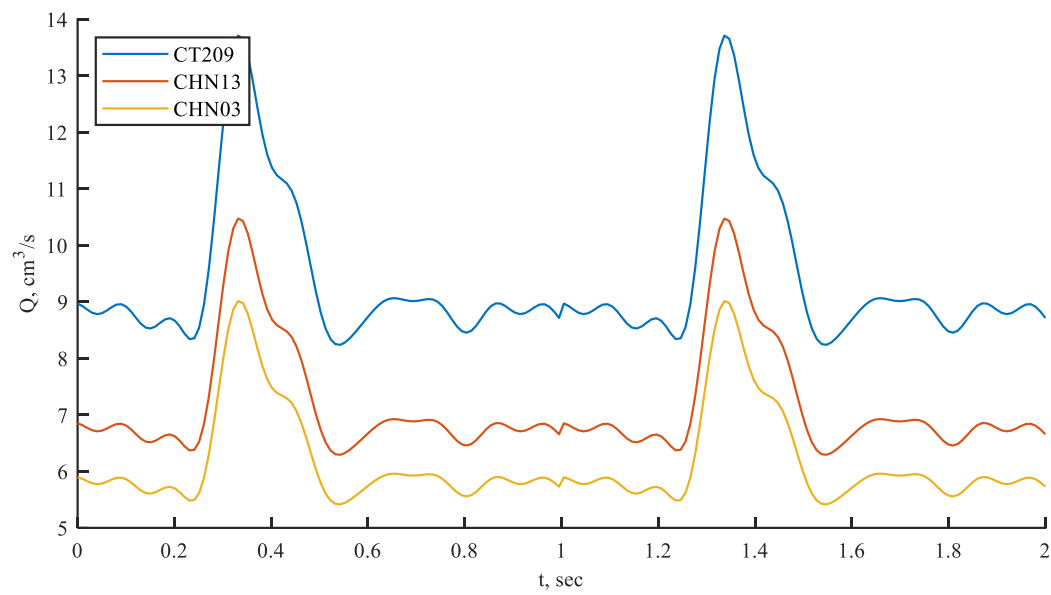
Murray's law calculation for outlet flow rates					
	A_i (cm ²)	d_i (cm)	d_i^3 (cm ³)	α_i	Q_i (cm ³ /s)
outlet 1	1.674	1.46	3.111	0.082	0.769
outlet 2	4.105	2.286	11.948	0.314	2.955
outlet 3	1.802	1.515	3.475	0.091	0.859
outlet 4	0.977	1.116	1.388	0.037	0.343
outlet 5	1.398	1.334	2.374	0.062	0.587
outlet 6	4.114	2.289	11.988	0.315	2.965
outlet 7	0.925	1.085	1.279	0.034	0.316
outlet 8	0.568	0.851	0.616	0.016	0.152
outlet 9	1.173	1.222	1.824	0.048	0.451

Table 6. Initial calculated flow rates at each outlet by Murray's law for CHN13 [21]

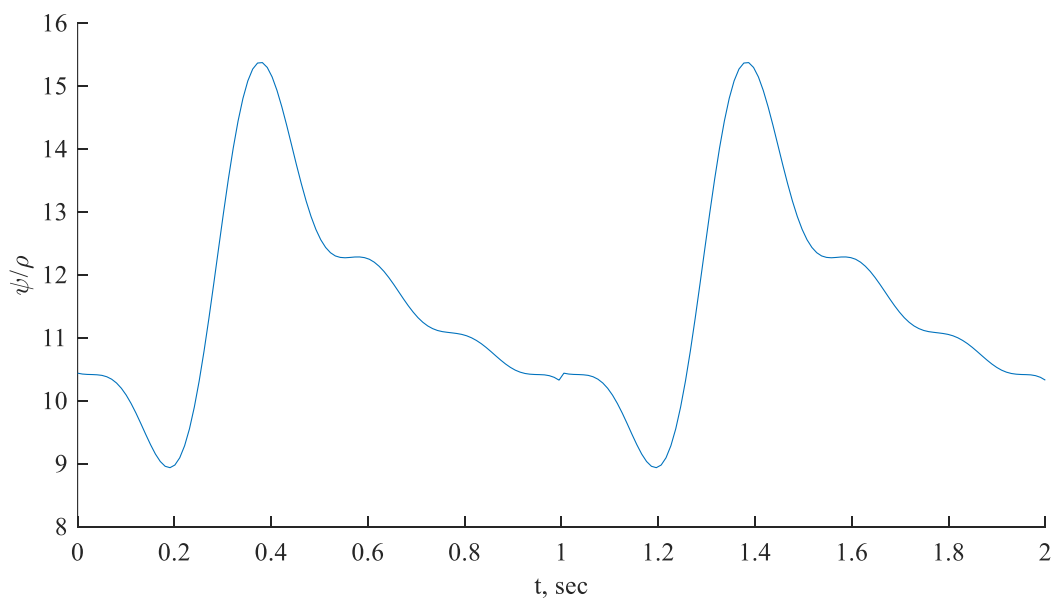
Murray's law calculation for outlet flow rates					
	A_i (cm ²)	d_i (cm)	d_i^3 (cm ³)	α_i	Q_i (cm ³ /s)
outlet 1	2.712	1.858	6.418	0.227	1.630
outlet 2	1.832	1.527	3.564	0.126	0.905
outlet 3	1.005	1.131	1.447	0.051	0.368
outlet 4	1.950	1.576	3.913	0.139	0.994
outlet 5	1.969	1.583	3.970	0.141	1.009
outlet 6	3.382	2.075	8.936	0.316	2.270

Table 7. Initial calculated flow rates at each outlet by Murray's law for CHN03 [21]

Murray's law calculation for outlet flow rates						
	i	A_i (cm ²)	d_i (cm)	d_i^3 (cm ³)	α_i	Q_i (cm ³ /s)
outlet 1	1	2.5675	1.8081	5.9106	0.2240	1.3847
outlet 2	2	2.2262	1.6836	4.7721	0.1808	1.1179
outlet 3	3	2.1930	1.6710	4.6658	0.1768	1.0930
outlet 4	4	1.8206	1.5225	3.5293	0.1338	0.8268
outlet 5	5	1.7784	1.5048	3.4074	0.1291	0.7982
outlet 6	6	2.0126	1.6008	4.1021	0.1555	0.9610



(a)



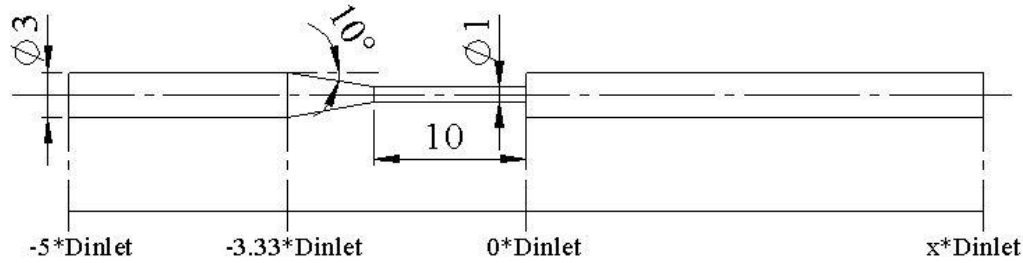
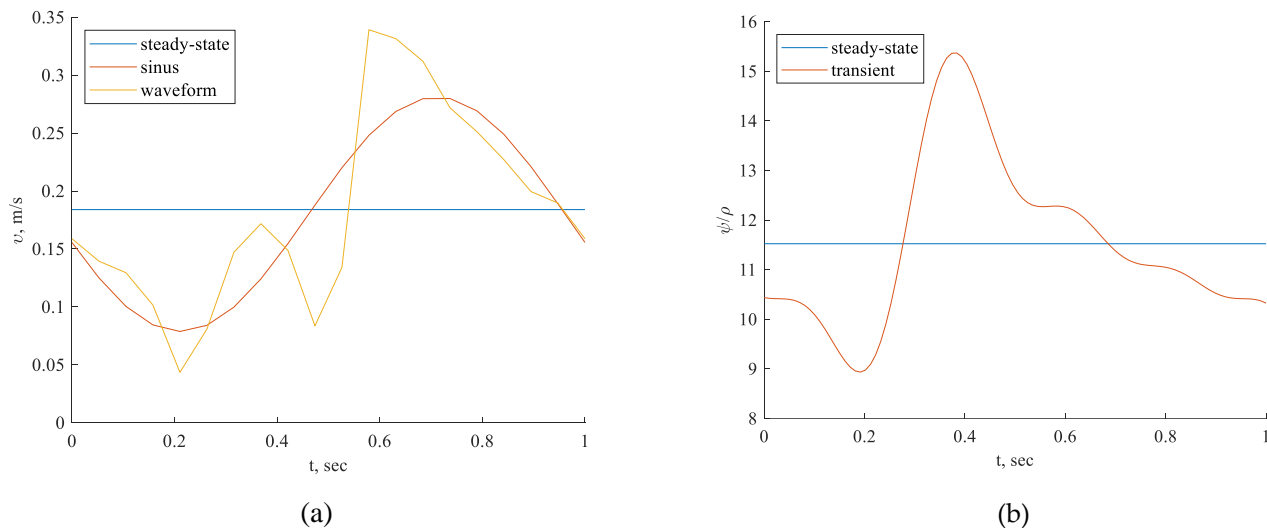
(b)

Figure 6. Inlet boundary conditions: transient flow rate (a) and normalized pressure (b) waveform of coronary blood flow.

The PBA study was replicated on the FDA benchmark model to validate the PBA approach. The nozzle geometry used in this study is shown in Figure 7 and has been previously described in detail by Stewart et al. [17-18]. The original FDA nozzle has a 12 mm-diameter inlet and outlet tube, with a throat-to-inlet tube ratio of 1/3. Stiehm et al. scaled down the nozzle geometry to a 3 mm tube diameter. The normalization of the results was done to ensure comparability with the outcomes of the FDA's round-robin trial. The FDA nozzle in this study only used one cycle, as the same boundary conditions were already tested by Stiehm et al [19].

Table 8. Experimentally obtained input parameters for simulation for FDA nozzle [18]

Parameter	Value
Experimental inlet pressure P_{exp}	63.61 mm Hg (8,480 Pa)
Experimental inlet flow rate v_{exp}	0.184 m/s

**Figure 7.** Geometry of coronary nozzle [16].**Figure 8.** a) Inlet boundary conditions: steady state velocity, waveform of left main coronary blood flow (adapted from [14]) and sinus flow: $u(t) = 0.184\text{m/s} - 0.02432\text{m/s} \cdot \cos(2\pi \cdot t) - 0.09822\text{m/s} \cdot \sin(2\pi \cdot t)$, b) Inlet boundary conditions: normalized steady state pressure, normalized transient waveform pressure.

The convergence criteria are evaluated at the end of each iteration with equation (13). The procedure presented in Table 1 is repeated continuously until the convergence is achieved. FFR is computed using the formula (13).

$$FFR = \frac{\min(P_1, P_2, \dots, P_n)}{P_{exp}} \quad (13)$$

3. Results and Discussion

The mesh generation for the blood vessels was done using the open-source CFmesh utility, which is part of OpenFOAM and generates volumetric meshes of unstructured Cartesian type. CFmesh is also able to automatically generate tetrahedral meshes for a variety of geometries, as shown in Fig. 9. Mesh sensitivity analysis was conducted [18], and the same models were used in this study. For the arteries CT209, CHN13, and CHN03, our research group [21] selected mesh sizes of 0.17mm, 0.22mm, and 0.2 mm, respectively, based on the results of the mesh sensitivity analysis.

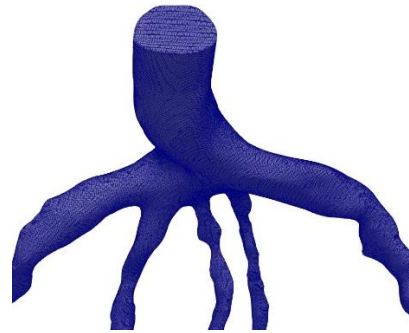
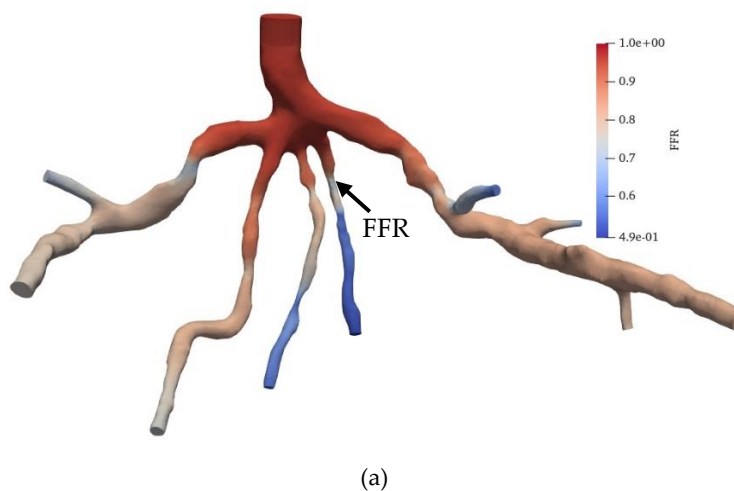


Figure 9. Cartesian mesh example

FFR is calculated using equation 13, and for the CT209 model, it has an experimental value of 0.76 [20]. Fig. 10 shows the derived FFR values from the most recent iteration, along with the relative percentage difference between the computed and experimental FFR (the degree of deviation from the experimentally obtained FFR). The calculated non-invasive FFR value of 0.73 by Zhang et al. [17] is different from the experimental (ICA) FFR value of approximately 0.76 for the CT209 model. After conducting mesh sensitivity analysis, Sumbekova et al. [21] from our research group obtained final FFR values of FFR=0.757, which was very close to the ICA FFR. The same algorithm implemented in OpenFOAM produced results that were similar to the ICA measurement, with final FFR values of FFR=0.762.

According to Zhang et al. [20], the Left Anterior Descending (LAD) Proximal artery is the site of arterial stenosis in the CT209 model [20]. In Fig. 10, the LAD Proximal is the dark blue area of the blood artery, and it is observed that the artery stenosis is in the same location as identified by Zhang et al. [20]. Fig. 10a includes the visualized FFR findings from the tenth iteration of the steady-state PBA.



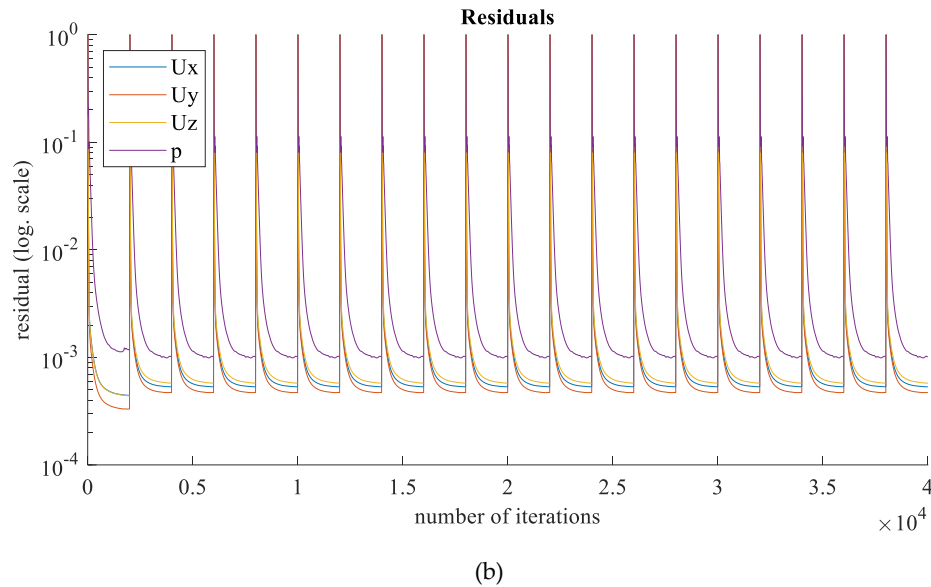
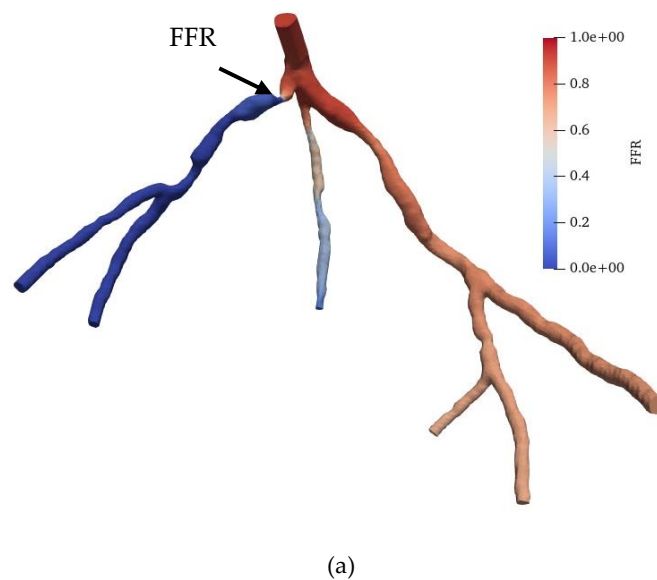


Figure 10. a) FFR distribution along with the shape of CT209 steady-state PBA model and b) PBA residual history

We compared the **steady-state** results obtained by the PBA method in OpenFOAM with those obtained using the traditional lumped parameter method and the current approach used by our research group [21], as well as with the ICA measurement results. It was found that the PBA method demonstrates good accuracy and efficiency, similar to the traditional methods. Figs. 11 and 12 show the visualized FFR distributions for the CHN13 and CHN03 models, respectively. The calculated FFRs for CHN03 and CHN13 by the OpenFOAM PBA are 0.88 and 0.683, respectively, which are in excellent agreement with the corresponding experimental values of 0.86 and 0.68.

Figs. 13-15 show the FFR distributions in transient simulations for the CT209, CHN13, and CHN03 models, respectively. The PBA residuals also demonstrate convergence in the velocity and pressure equations.



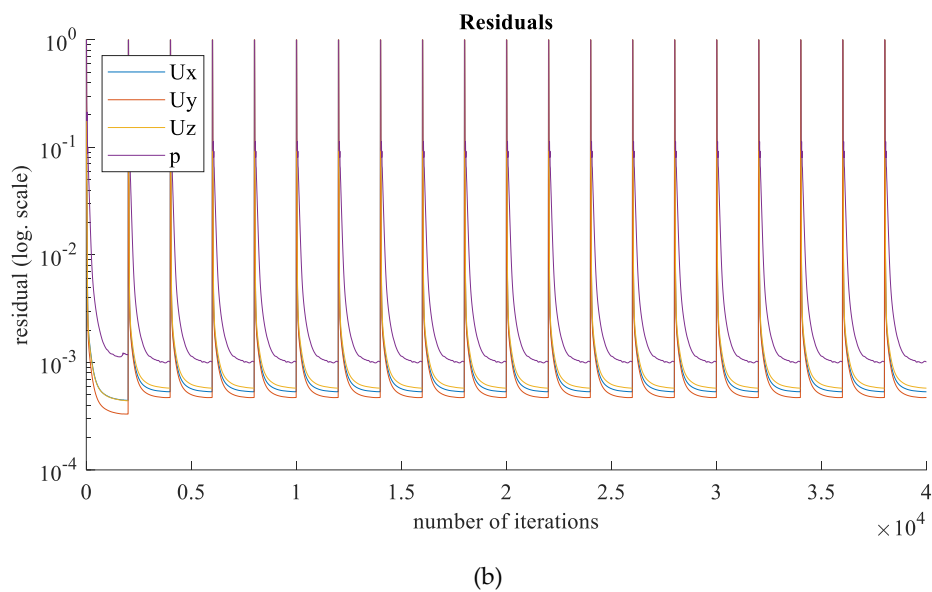


Figure 11. a) FFR distribution along with the shape of CHN13 steady-state PBA model and b) PBA residual history

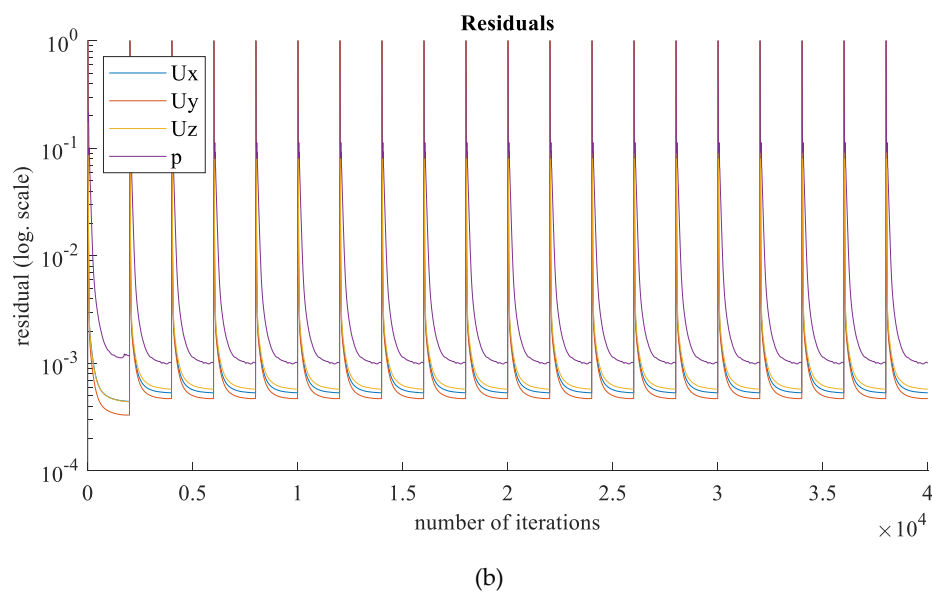
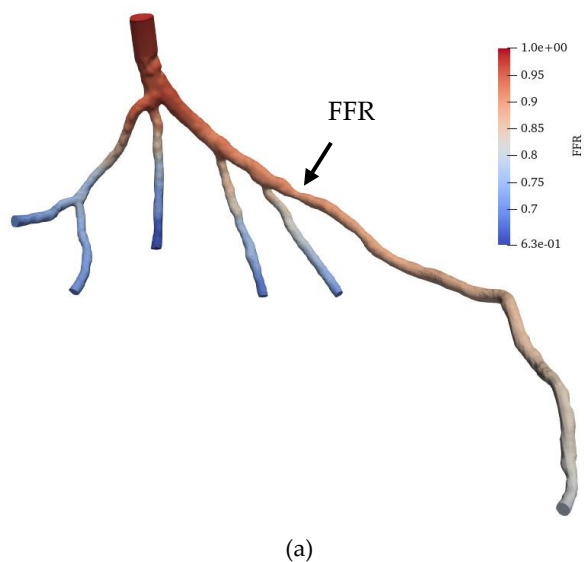


Figure 12. a) FFR distribution along with the shape of CHN03 steady-state PBA model and b) PBA residual history

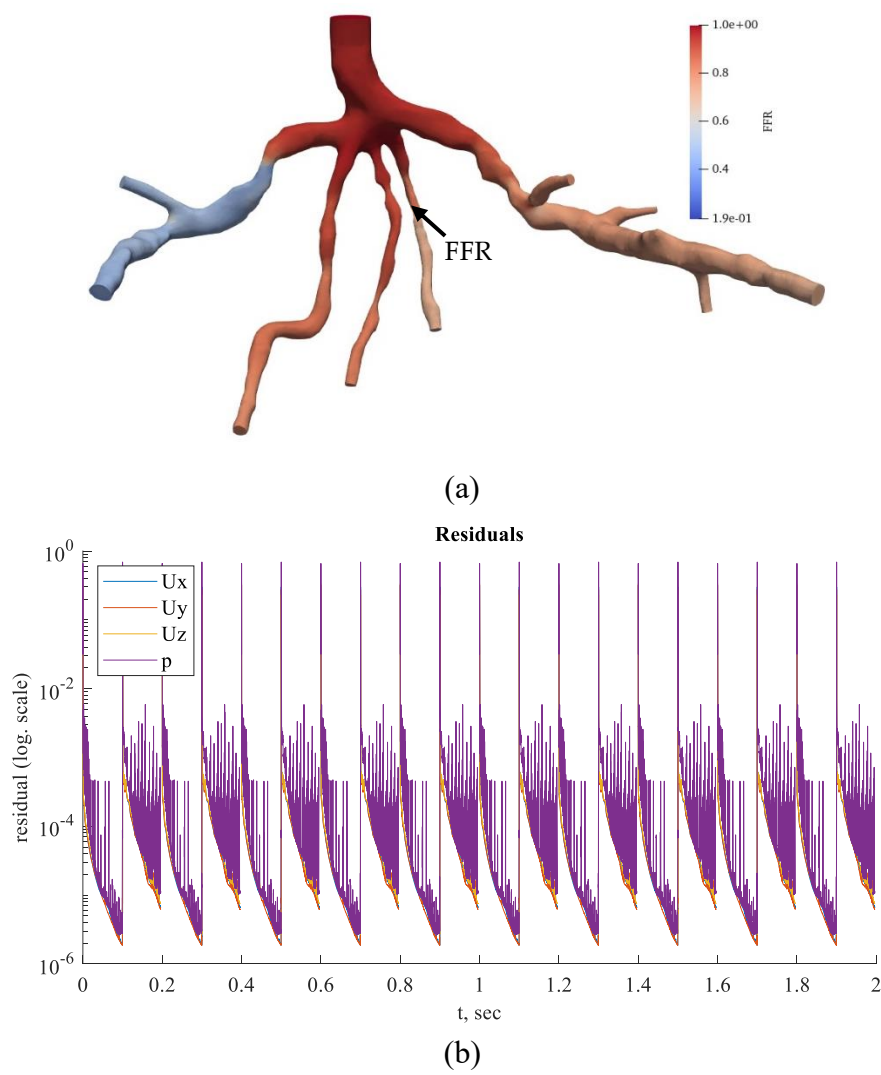
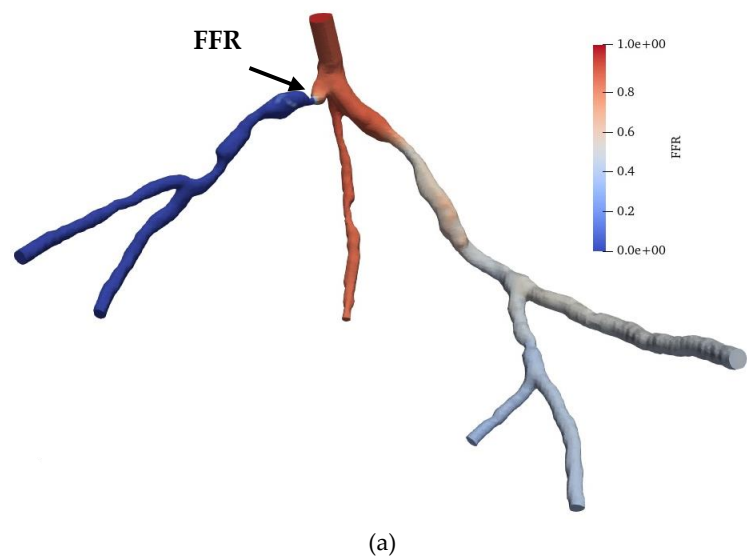


Figure 13. a) FFR distribution along with the shape of CT209 **transient** PBA model and b) PBA residual history



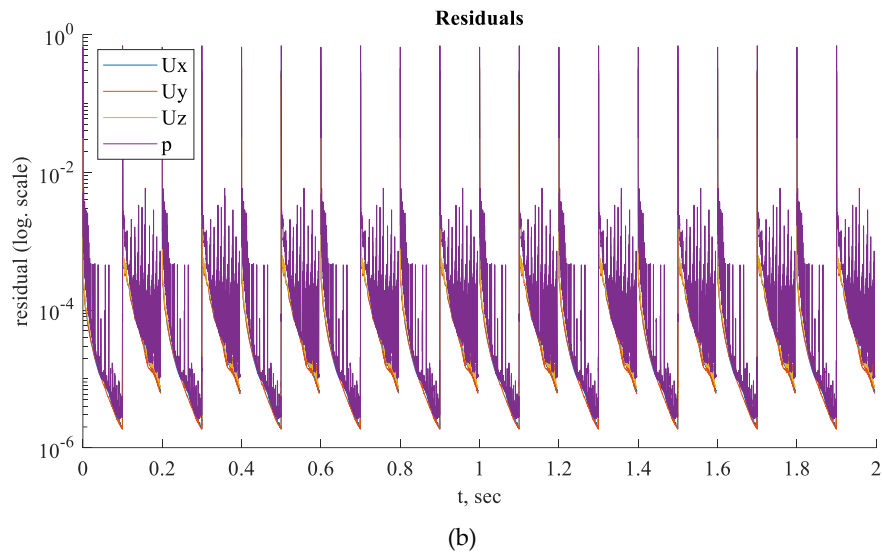


Figure 14. a) FFR distribution along with the shape of CHN13 transient PBA model and b) PBA residual history

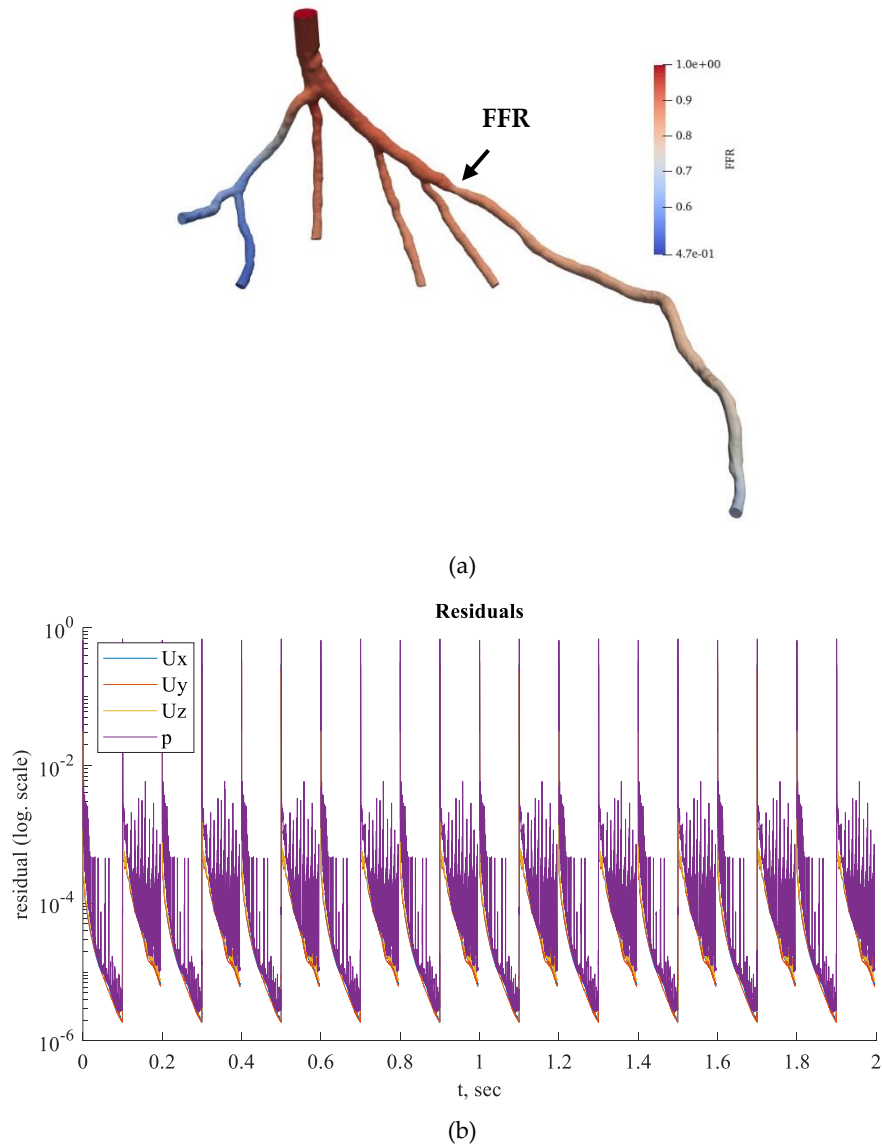
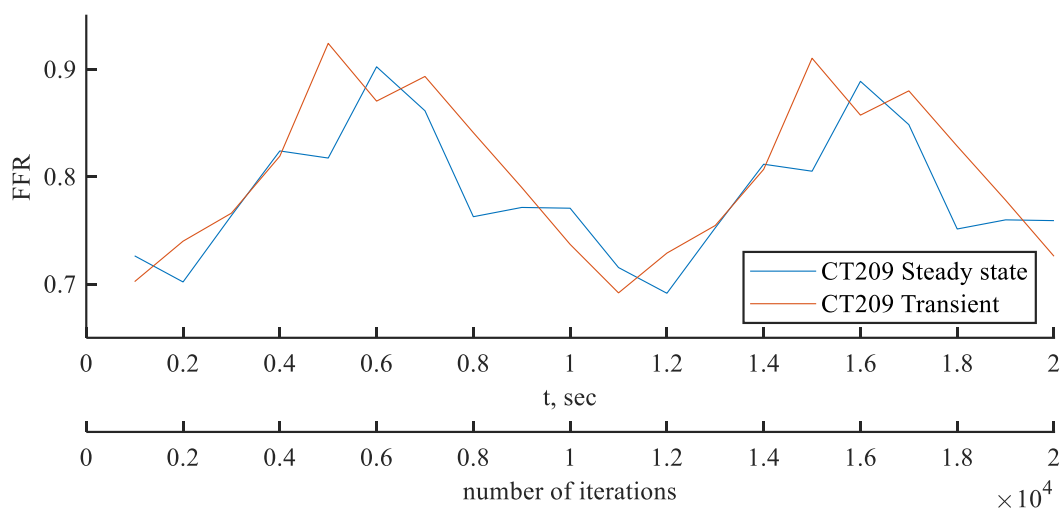
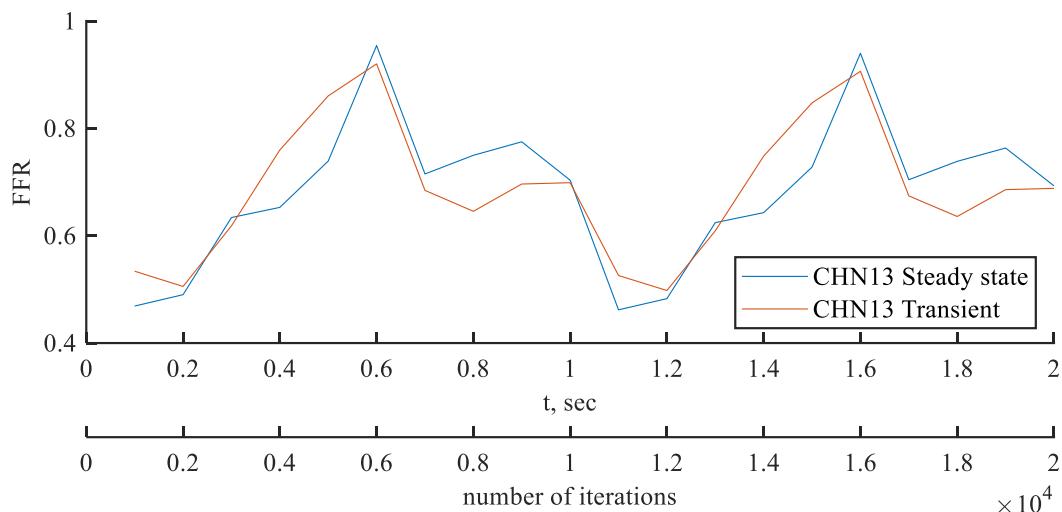


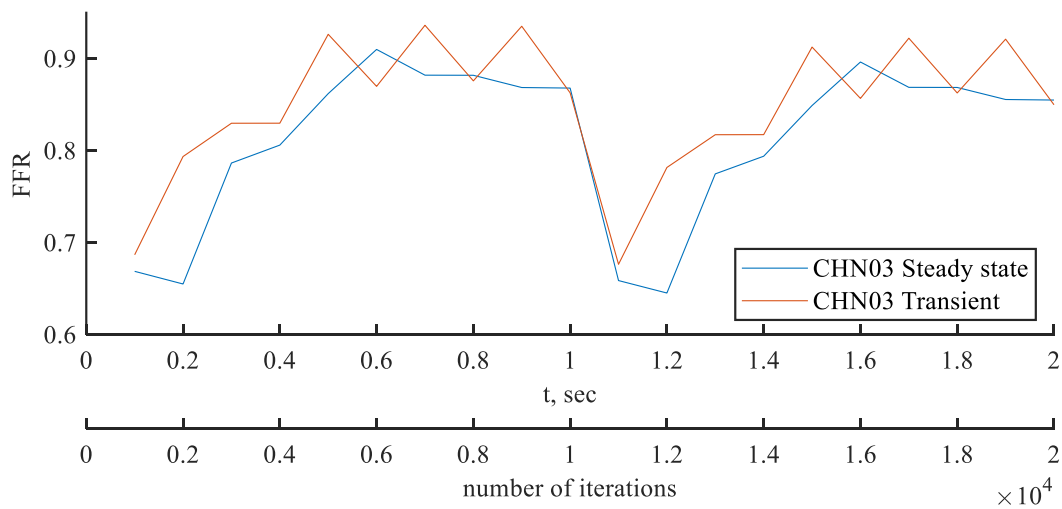
Figure 15. a) FFR distribution along with the shape of CHN03 transient PBA model and b) PBA residual history



(a)



(b)



(c)

Figure 16. a) FFR probe values comparison between **steady state** and **transient** PBA models for a) CT209, b) CHN13 and c) CHN03

Preliminary steady-state simulations were conducted to achieve convergence of the model before performing OpenFOAM transient PBA simulations using the mapFields package. The mapFields utility converts one or more fields that are specific to a geometry into their equivalents, and it is universal because there is no requirement for the geometries to be similar [22].

In Figs. 13b-15b, during iterations, the PBA method switches the boundary conditions, which can lead to high-frequency oscillations. For transient simulations, it is necessary to drive the solution to convergence at each time step, which results in fluctuations that appear to have a high frequency. The solution may exhibit wave reflections resembling high-frequency oscillations due to the complex geometry. Figure 16 compares the FFR values between steady-state and transient simulations at the locations indicated by the FFR arrows in Figures 11-15. The FFR values increase in all three scenarios and tend to decrease due to alignment with the flow rate waveform.

The mean FFR values are included in Table 9 as the outcome value for transient simulations. As shown in Fig. 16c, the second half of the transient instance exhibits rapid fluctuations in the FFR due to changes in the PBA boundary conditions. In Figs. 16a and 16b, the models show good agreement with the flow rate inputs, indicating that the PBA method may converge over several flow rate cycles.

Table 9. Relative errors calculated between the invasive and calculated FFRs by Simvascular, Ansys CFX and OpenFOAM.

model	Calculated FFR				Invasive FFR	Relative error, %			
	Ansys CFX	Simvascular	OpenFOAM Steady-state PBA	OpenFOAM Transient PBA		Ansys CFX	Simvascular	OpenFOAM Steady-state PBA	OpenFOAM Transient PBA
CT209	0.753	0.758	0.762	0.80	0.76	0.92	0.26	0.26	5.26
CHN03	0.87	0.872	0.86	0.859	0.86	1.16	1.38	2.33	0.02
CHN13	0.658	0.691	0.683	0.69	0.68	3.24	1.59	0.44	1.47

Three artery models were analyzed using both methods: the standard LPM technique was used in ANSYS [21], while the suggested PBA was implemented in Simvascular [21] and OpenFOAM for steady-state and transient cases, respectively, as described in Appendix A and B.

Table 9 provides a summary of the comparison between the computed and experimental ICA FFRs [21]. This table shows that the recommended PBA produces results that are independent of the solver. Simvascular and OpenFOAM were used for the suggested PBA, while ANSYS was used for the conventional LPM approach.

The findings indicate that the relative errors or discrepancies across steady-state simulations in ANSYS CFX, Simvascular, and OpenFOAM do not exceed 3.24%. The results also show that the relative error disparities in transient simulations in OpenFOAM do not exceed 5.26%. The smallest inaccuracy was observed in Simvascular and OpenFOAM steady-state PBA for CT209, at 0.26%. The largest inaccuracy for CT209 was in the OpenFOAM transient PBA, at 5.26%. This may be due to the highest flow rate values, which could increase the overall FFR readings in the tested artery. The error in OpenFOAM transient PBA for CHN03 was the smallest recorded, at 0.02%, while the largest inaccuracy for CHN03 was in the OpenFOAM steady-state PBA, at 2.33%. The error in OpenFOAM steady-state PBA for CHN13 was the lowest, at 0.44%, while the highest error was in ANSYS CFX, at 3.24%. Despite the error peaks associated with various methods, the PBA approach shows promising performance.

The classic LPM and LPNM techniques, which involve the calculation of capacitance, resistance, inductance, and the creation of a fictitious downstream capillary vessel network using fractal techniques, are fundamentally different from the PBA approach. The LPM and LPNM techniques require the calculation of resistance at the outlets and the use of additional inlet measurement conditions and numerical iterations, which are not based purely on physiology. In contrast, the PBA technique is patient-specific and physiologically based. It estimates the initial conditions at the outlets using Murray's law and then uses the geometry of the arterial tree, the conservation laws incorporated into CFD, the suggested numerical iteration scheme, and the additional measured inlet patient-specific conditions to determine the final conditions at the outlets. The suggested PBA strategy, which is completely based on physics and physiology and is patient-specific, has also been shown to be computationally effective. It is integrated into the standard CFD pressure correction iterations as an iterative boundary-switching system that does not require two simulation rounds.

The PBA approach was further validated using the standard LPM method published in Zhang et al. [20] for real-patient arteries. The LPM method employs a reference pressure, resistances at every outlet representing the flow resistance from the downstream microvasculature, and an overall resistance for the entire CAT that is related to the outlet resistances through a population-averaged empirical scaling law [20]. The LPM is an iterative procedure that calculates the resistances and reference pressure to determine the outlet pressures in each branch outlet. It has been found that the LPM does not always ensure convergence to a unique solution for every situation. In contrast, the suggested PBA also achieves convergence to precise answers for all three analyzed scenarios. The PBA approach is more reliable than the LPM because it is physiologically based and patient-specific, while the LPM does not consider these characteristics.

Additionally, the PBA approach was verified using the benchmark model of the FDA nozzle. The goal was to replicate the study by Stiehm et al. [19] using the PBA approach. The computational results of the axial velocity along the centerline of the nozzle geometry were compared to the CFD data from the FDA's round-robin study [19] for validation. The inlet conditions, shown in Figures 7-8, were the same as in the Stiehm et al. [19] study. The FFR distribution along the profile of the FDA nozzle can be seen in Fig. 17, but we used the velocity results along the centerline for validation.

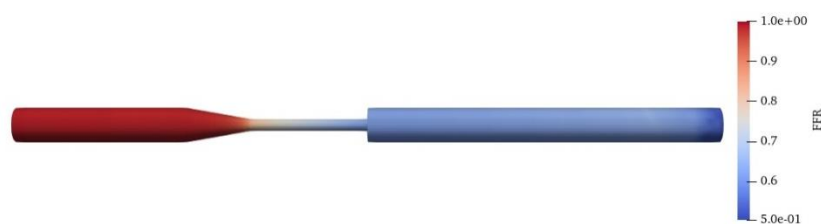


Figure 17. FFR distribution along with the shape of FDA nozzle model

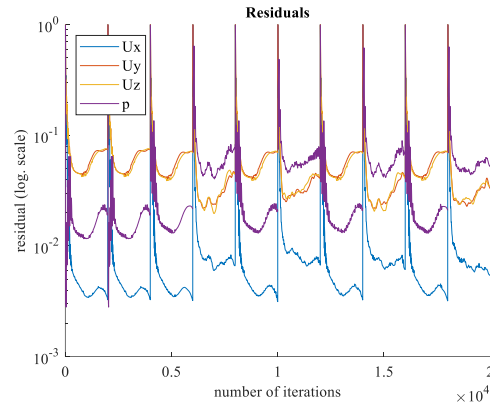


Figure 18. Residual history for **steady-state** along with the shape of FDA nozzle model

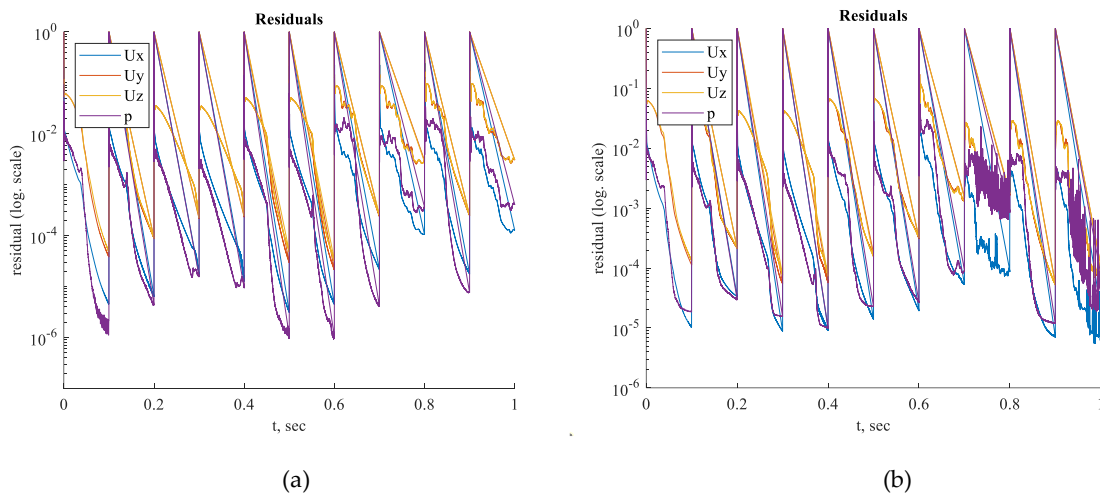


Figure 19. Residual histories for transient sinus (a) and waveform (b) along with the shape of FDA nozzle model

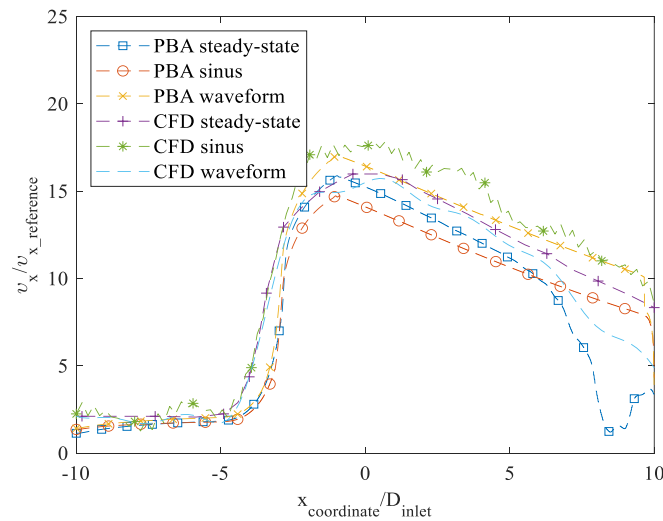


Figure 20. Axial flow rate along nozzle centreline: CFD results under steady state and transient conditions and CFD PBA results under steady state and transient conditions.

Residual values for steady-state and transient simulations are shown in Figures 18 and 19, respectively. Based on the appropriate convergence of the residual values, the findings can be considered acceptable.

The axial velocity results for the CFD steady-state and CFDPBA databases for the idealized FDA nozzle match closely, as shown in Figure 20. Additionally, the time-averaged axial velocity obtained from the transient CFD simulation with waveform inlet conditions agrees well with the steady-state PBA velocity data. However, there are minor differences downstream of the nozzle between 5D and 10D (Fig. 7). The inclusion of wave pressure in the PBA algorithm causes the PBA sinus and waveform deviation. Since the pressure is constant in the steady-state example, the findings are not affected, but the waveform pressure causes a slight fluctuation in the centerline velocity values.

4. Conclusions

In this work, a physiologically based algorithm (PBA) was proposed and implemented in the OpenFOAM CFD solver to simulate blood flow in three coronary artery tree models and the FDA nozzle model. The performance of the proposed PBA was assessed using OpenFOAM and other CFD solvers [21]. The PBA, which is based on Murray's law and patient-specific conditions at the inlet, can accurately calculate the outlet boundary conditions iteratively, a task that is difficult for both traditional LPM methods and invasive measurement. The PBA was found to work well with all the CFD solvers, such as Simvascular and OpenFOAM, and it can accurately predict FFR values in the cases tested. The results of the PBA were also compared with the LPM method, which was performed in ANSYS CFX [21]. The FFR values obtained from simulations using the suggested PBA are in excellent agreement with experimental ICA measurements. Unlike traditional methods, the PBA always guarantees quick convergence in steady-state cases to an accurate solution for every situation. Because it is significantly more accessible and effective than the conventional Windkessel circuit analogy technique, this noninvasive FFR estimate using the PBA is a potential strategy for patient-specific detection of coronary stenosis. Our study further suggests that the suggested PBA, combined with an effective CFD solver, can be used as a low-cost, effective, and precise tool for diagnosing CAD. In individual patients, the PBA method has the potential to replace the expensive and risky invasive coronary angiography (ICA) procedure. Future research on pulsatile flows in CATs with fluid-structure interaction using the PBA is suggested.

We also used a nozzle model in this work that is based on the FDA's benchmark geometry. By comparing the estimated axial velocity profile to CFD and CFDPBA data provided by the FDA, normalized fluid mechanical quantities can be used to further validate the method and its results.

Finally, two different transient CFD simulations were performed utilizing a sinus inlet condition and a physiological waveform. We conclude that if only time-averaged results are examined, steady-state simulations are appropriate for hemodynamic studies. This approach may reduce the need for computing resources in further hemodynamic studies.

Acknowledgments: The authors would like to acknowledge the assistance and supply of the CT209, CHN13, and CHN03 models by Dr. Zhong Liang of NHCS, as reported in [17]. The authors also want to acknowledge Jozsef Nagy for the OpenFOAM tutorials.

References

1. World Health Organization. 2018. World Health Organization - Noncommunicable Diseases (NCD) Country Profiles, 2018. https://www.who.int/nmh/countries/kaz_en.pdf?ua=1.
2. Roger VL, Go AS, Lloyd-Jones DM et al. Executive summary: heart disease and stroke statistics—2012 update: a report from the American Heart Association. *Circulation* 2012;124:188–97
3. Bjarne L. Nørgaard, Jonathon Leipsic, Sara Gaur, Sujith Seneviratne, Brian S. Ko, Hiroshi Ito, Jesper M. Jensen, Laura Mauri, Bernard De Bruyne, Hiram Bezerra, Kazuhiro Osawa, Mohamed Marwan, Christoph Naber, Andrejs Erglis, Seung-Jung Park, Evald H. Christiansen, Anne Kaltoft, Jens F. Lassen, Hans Erik Bøtker, Stephan Achenbach, Diagnostic Performance

- of Noninvasive Fractional Flow Reserve Derived From Coronary Computed Tomography Angiography in Suspected Coronary Artery Disease: The NXT Trial (Analysis of Coronary Blood Flow Using CT Angiography: Next Steps), *Journal of the American College of Cardiology*, Volume 63, Issue 12, 2014, Pages 1145-1155, ISSN 0735-1097, <https://doi.org/10.1016/j.jacc.2013.11.043>.
4. Chen, Z. (2021). Role of coronary CT imaging diagnosis of coronary functional stenosis. *Journal of Image Processing Theory and Applications*, 4(1), 38-41.
 5. Fabio Mangiacapra, Edoardo Bressi, Alessandro Sticchi, Carmine Morisco & Emanuele Barbato (2018) Fractional flow reserve (FFR) as a guide to treat coronary artery disease, *Expert Review of Cardiovascular Therapy*, 16:7, 465-477, DOI: [10.1080/14779072.2018.1489236](https://doi.org/10.1080/14779072.2018.1489236)
 6. Li, C., Xu, R., Yao, K. et al. Functional significance of intermediate coronary stenosis in patients with single-vessel coronary artery disease: A comparison of dynamic SPECT coronary flow reserve with intracoronary pressure-derived fractional flow reserve (FFR). *J. Nucl. Cardiol.* 29, 622–629 (2022). <https://doi.org/10.1007/s12350-020-02293-z>
 7. De Bruyne B et al. 2012. "Fractional Flow Reserve–Guided PCI versus Medical Therapy in Stable Coronary Disease". *New England Journal of Medicine* 367 (11): 991-1001. Massachusetts Medical Society. doi:10.1056/nejmoa1205361.
 8. Secchi F et al. 2016. Fractional flow reserve based on computed tomography: an overview. *European Heart Journal Supplements* 2016 18 (Supplement E), E49–E56, doi:10.1093/eurheartj/suw014
 9. Nakanishi R, Budoff MJ. Noninvasive FFR derived from coronary CT angiography in the management of coronary artery disease: technology and clinical update. *Vasc Health Risk Manag.* 2016 Jun 22;12:269-78. DOI: 10.2147/VHRM.S79632. PMID: 27382296; PMCID: PMC4922813.
 10. Xie, X., Zheng, M., Wen, D. et al. A new CFD based noninvasive method for functional diagnosis of coronary stenosis. *Bio-Med Eng OnLine* 17, 36 (2018). <https://doi.org/10.1186/s12938-018-0468-6>
 11. Kim H J, Vignon-Clementel I E, Coogan J S, Figueroa C A, Jansen K E, and Taylor C A 2010. Patient-specific modeling of blood flow and pressure in human coronary arteries. *Annals of biomedical engineering*, 38(10), 3195-3209.
 12. Murray C D 1926. The Physiological Principle of Minimum Work: I. The Vascular System and the Cost of Blood Volume. *Proceedings of the National Academy of Sciences of the United States of America*. 12 (3): 207–214. doi:10.1073/pnas.12.3.207. PMC 1084489. PMID 16576980
 13. Patankar, S. V. (1980). *Numerical Heat Transfer and Fluid Flow*. Taylor & Francis. ISBN 978-0-89116-522-4.
 14. Zamir, M., & Brown, N. (1983). Internal geometry of arterial bifurcations. *Journal of biomechanics*, 16(10), 857-863.
 15. VanBavel, E., & Spaan, J. A. (1992). Branching patterns in the porcine coronary arterial tree. Estimation of flow heterogeneity. *Circulation research*, 71(5), 1200-1212.
 16. Kaimovitz, B., Huo, Y., Lanir, Y., & Kassab, G. S. (2008). Diameter asymmetry of porcine coronary arterial trees: structural and functional implications. *American Journal of Physiology-Heart and Circulatory Physiology*, 294(2), H714-H723.
 17. Stewart SFC, Hariharan P, Paterson EG, Burgreen GW, Reddy V, Day SW, Giarra M, Manning KB, Deutsch S, Berman MR, Myers MR, Malinauskas RA. Results of FDA's First Interlaboratory Computational Study of a Nozzle with a Sudden Contraction and Conical Diffuser. *Cardiovascular Engineering and Technology*. 2013, 4(4), pp. 374–391
 18. Stewart SFC, Paterson EG, Burgreen GW, Hariharan P, Giarra M, Reddy V, Day SW, Manning KB, Deutsch S, Berman MR, Myers MR, Malinauskas RA. Assessment of CFD Performance in Simulations of an Idealized Medical Device: Results of FDA's First Computational Interlaboratory Study. *Cardiovasc. Eng. Technol.* 2012. 3(2), pp. 139–160.
 19. Stiehm, M., Wüstenhagen, C., Siewert, S., Grabow, N., & Schmitz, K. P. (2017). Numerical simulation of pulsatile flow through a coronary nozzle model based on FDA's benchmark geometry. *Current Directions in Biomedical Engineering*, 3(2), 775-778.
 20. Zhang J M et al. 2016. "Simplified Models of Noninvasive Fractional Flow Reserve Based on CT Images." *PLOS ONE* 11 (5): e0153070. Public Library of Science (PLOS). doi:10.1371/journal.pone.0153070.
 21. Sumbekova, S., Maldenov, N., Zhamiyev, A., Tianqi, Y., Xiaohui, S., & Zhao, Y. A Novel Physiologically Based Algorithm (PBA) for Fast CFD Computation of Flow Fractional Reserve (FFR) in Coronary Artery Trees, *Medical Engineering & Physics* (under review), 2022
 22. OpenFOAM. Available online: <https://www.openfoam.com/> (accessed on 20 September 2021).